Vacancy in silicon: Hyperfine interactions from electron-nuclear double resonance measurements

M. Sprenger,* S. H. Muller, E. G. Sieverts, and C. A. J. Ammerlaan
Natuurkundig Laboratorium der Universiteit van Amsterdam, Valckenierstraat 65, 1018 XE Amsterdam, The Netherlands
(Received 14 April 1986)

The isolated vacancy in silicon has been studied with magnetic resonance spectroscopy. The EPR spectrum labeled Si-G2, identified as arising from the negative charge state of the vacancy, has been investigated by electron-nuclear double resonance. Hyperfine interactions between the unpaired defect electron and ^{29}Si nuclei were determined for 51 shells of surrounding atoms. These shells contain 152 lattice sites. They can be divided into four different symmetry classes. From a linear combination of atomic orbitals (LCAO) analysis of the hyperfine interactions together with the division in classes, we found that the defect wave function is primarily localized in one mirror plane of the vacancy. In this plane it could especially be assigned to lattice sites on a particular ⟨011⟩ lattice chain. This one-dimensional character of the defect confirms the preference for charge transfer along ⟨011⟩ chains which was found in theoretical calculations. This picture leads to the identification of hyperfine interactions with atoms in the chain and tentatively even in a side chain. The very small localization on the other mirror plane of the vacancy is in agreement with a one-electron defect-molecule description which predicts it to be a nodal plane of the wave function. The remaining small localization allows an estimate of the importance of many-electron effects. Because of this small localization, small discrepancies of the LCAO description become prominent in this plane. In a number of cases dipole-dipole interaction with spin density on nearby lattice sites can explain the observed hyperfine interactions. Also exchange polarization effects have to be considered there. The positive charge state of the vacancy has been studied with EPR only. Incomplete hyperfine data for three shells of lattice sites are reported.

I. INTRODUCTION

A. General

The lattice vacancy is, by its nature, one of the most important defects in silicon, certainly from a theoretical point of view. It is the simplest lattice defect that is known and it is the primary defect that is produced upon irradiation with energetic particles. As vacancies are highly mobile, experiments on the isolated species require both their production and their observation to take place at low temperatures. As this imposes rather severe requirements on the experimental equipment, only few experimental studies of the vacancy have been performed up to now. The first observations of the vacancy in silicon by magnetic resonance date back to 1963.[1] Watkins observed a new EPR spectrum in low-temperature irradiated silicon and ascribed it to the positively charged vacancy. Later this spectrum was labeled Si-G1 according to the labeling scheme for defect spectra in silicon which he introduced.[2] Another EPR spectrum, labeled Si-G2, was associated with the vacancy in its negatively charged state.[2]

The identification of these two EPR spectra Si-G1 and Si-G2 with V^+ and V^-, respectively, was strongly supported by a one-electron molecular orbital treatment of the vacancy.[2,3] In this treatment the four atomic orbitals of the broken bonds on the atoms around the vacancy formed the defect molecule. A tetragonal or trigonal Jahn-Teller distortion was predicted for V^+ and V^0 and a lower symmetry orthorhombic distortion for V^-. The experiments were consistent with these predictions. Figure 1 shows a model of the vacancy in its positive and negative charge states. In Fig. 2 the level scheme of the one-electron molecular orbital treatment is given. In the case of V^+ the paramagnetic electron occupies a molecular orbital wave function of the form $a+d-c-b$; in the case

TABLE I. g values of the vacancy in its two paramagnetic charge states, taken from Ref. 2. Also included are thermal anneal characteristics from Ref. 4.

Spectrum	Model	Point-group Symmetry	g values g_1, $\|\|\langle 100\rangle$	g_2	g_3	Anneal temperature (K)
Si-G1	V^+	$\bar{4}2m$	2.0087	1.9989	1.9989	150–180
Si-G2	V^-	$2mm$	2.0038	2.0028	2.0151	60

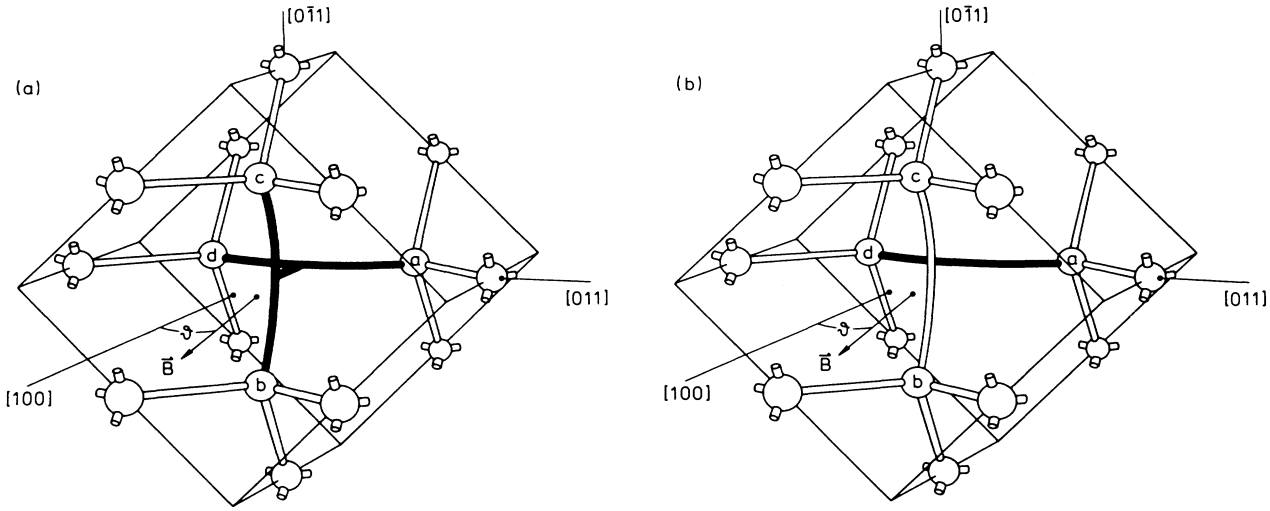

FIG. 1. Models of the vacancy in its two paramagnetic charge states: (a) V^+, the tetragonal Jahn-Teller distortion has lowered the symmetry to $\bar{4}2m$. (b) V^-, the symmetry is further lowered to $2mm$.

of V^- of the form $a-d$.[3]

Watkins also studied stress alignment, thermally activated reorientation, and annealing characteristics of both spectra.[4] Table I gives the g values and the anneal temperatures of the EPR spectra, as determined by Watkins.

Only recently, in a series of correlated EPR and deep-level transient-spectroscopy experiments, have Watkins and co-workers been able to solve some of the problems associated with the electrical level structure of the vacancy.[5–7] The charge states V^{2+}, V^+, and V^0 have been shown unambiguously to form an example of a so-called negative-U system. In such a system the addition of an electron will lower the total energy instead of raising it. This effect can, for instance, be caused when the energy gain of a Jahn-Teller distortion is larger than the repulsive energy of the electrons. In the case of the vacancy in silicon it means that the $(0/+)$ level lies below the $(+/++)$ level, with as its most striking consequence the fact that the V^+ charge state is metastable.

From a theoretical point of view, there has been an enormous interest in the single vacancy in elemental tetrahedral semiconductors (diamond, silicon, germanium). During the last 30 years, some 100 articles with theoretical calculations on this subject have been published. An overview with references to these papers has been published elsewhere.[8] Despite the proven importance of Jahn-Teller distortions in the vacancy system, because of calculational problems, many studies are performed on the undistorted lattice. Recently, Green's-function-type calculations proved rather successful, as they were able to predict the negative-U properties of the vacancy.[9–11] Since the number of experimental studies on the vacancy is an order of magnitude smaller, there is a tendency to compare theoretical results with each other, rather than with experimental data.

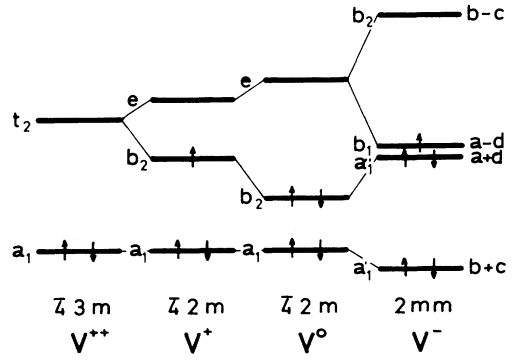

FIG. 2. Energy levels of the vacancy in a one-electron molecular orbital treatment. The various symmetry-lowering Jahn-Teller distortions from V^{++} ($\bar{4}3m$) to V^- ($2mm$) are indicated.

Important experimental information on the wave function of the unpaired electron in the paramagnetic charge states of the vacancy can be obtained from hyperfine interactions. The limited resolution of EPR experiments only allowed the largest hyperfine interactions to be measured. In the case of V^+, these are the interactions with the four nearest-neighbor atoms; for V^-, only with two of them. The present study was undertaken to exploit the much higher resolution of the electron-nuclear double resonance (ENDOR) technique in order to determine hyperfine interactions with more shells of silicon atoms and thus to obtain more detailed experimental information about the defect wave function. In the case of V^-, hyperfine interaction parameters with 152 neighboring atom sites, in 51 shells, could be determined from ENDOR experiments. These experimental results are presented in Sec. II and discussed in Sec. III. In the case of V^+, ENDOR could not be observed. Section IV gives a brief summary of these experiments. A more detailed description of the present work is given in Ref. 8. It forms a continuation of earlier ENDOR studies on the divacancy in silicon.[12,13]

B. Production of vacancies

Due to the high mobility of the vacancy all experiments were done in a cryostat which was especially designed for combined electron irradiation and magnetic resonance measurements at temperatures below 20 K.[8] We used p-type material, even for the production of negative vacancies, because it is well known that in p-type material the vacancy-production rate is higher by about an order of magnitude than in n-type material.[4] This effect is due to the high mobility of the self-interstitial in silicon (Si_I) under irradiation conditions, even at temperatures as low as 4 K. As a consequence, recombination of vacancies and interstitials occurs unless the latter are trapped elsewhere. Watkins showed in a number of publications that the substitutional acceptor elements act as such competitive traps and thus become interstitial themselves. This model was confirmed by the identification of two EPR spectra, Si-G18 and Si-G28, with Al_I (Refs. 2 and 14) and B_I (Ref. 15), respectively. The net vacancy production is about equal to the acceptor-interstitial production. Moreover, it was known that after prolonged irradiation of p-type material the stable charge state of the vacancy is V^-.

The ENDOR measurements on V^- were done on p-type Al-doped silicon with a resistivity of 0.9 Ω cm, containing 2×10^{16} Al atoms cm^{-3}. The dimensions of the sample were $\sim2\times2\times10$ mm^3. We irradiated the sample in several stages and monitored the EPR signals, in order to get the maximum possible intensity of Si-G2, together with a minimum intensity of other spectra that could disturb the ENDOR measurements. The irradiation temperature was kept well below 20 K, and after a total fluence of 10^{17} e^- cm^{-2}, V^- was the stable charge state of the vacancy. The vacancy concentration was roughly estimated from the EPR intensity to be $\sim10^{16}$ cm^{-3}. During the various stages several other spectra were observed, most of which are known from the literature. One new spectrum was seen and named Si-NL26. It is tentatively ascribed to some configuration of interstitial nitrogen.[16] Furthermore, Si-G18 was observed, as expected, because it is the interstitial aluminum atom. In the first stages of the irradiation we also observed Si-G1, the positively charged vacancy. The divacancy spectra Si-G6 (VV^+) and Si-G7 (VV^-) were seen but never exceeded an intensity of $\sim10^{15}$ cm^{-3}, as well as Si-G12 from interstitial carbon, and Si-G14, of unknown nature, but also seen by Watkins.[2] After the last irradiation we annealed to 42 K to remove spectrum Si-NL26.[16] The resulting spectrum of Si-G2 had about a 20 times higher intensity than any of the other remaining spectra, at a measuring temperature of 16—25 K. The production of positive vacancies is described in Sec. 4.

C. Magnetic resonance measurements

The EPR measurements on Si-G2 were performed with a superheterodyne spectrometer, operating at a microwave frequency of $\sim$23 GHz in dispersion mode, and at a temperature of 18 K. Figure 3 shows an example of an EPR spectrum. Clearly visible are the nearest-neighbor hyperfine interactions, the only ones that are fully resolved in EPR. Recording of the central part of the spectrum as a function of the angle of the magnetic field with respect to the [100] direction and subsequent fitting to the Hamiltonian $\mathscr{H}=\mu_B\mathbf{B}\cdot\vec{\mathbf{g}}\cdot\mathbf{S}$ with $S=\frac{1}{2}$ and $\vec{\mathbf{g}}$ a tensor with symmetry $2mm$ yields the g values. Figure 4 shows the angular dependence of the effective g values as calculated by the computer from the fitted values. The principal values of the $\vec{\mathbf{g}}$ tensor were determined to be $g_1=2.0039$, $g_2=2.0028$, and $g_3=2.0151$ (±0.0001), in close agreement with Watkins's values, as can be verified in Table I.

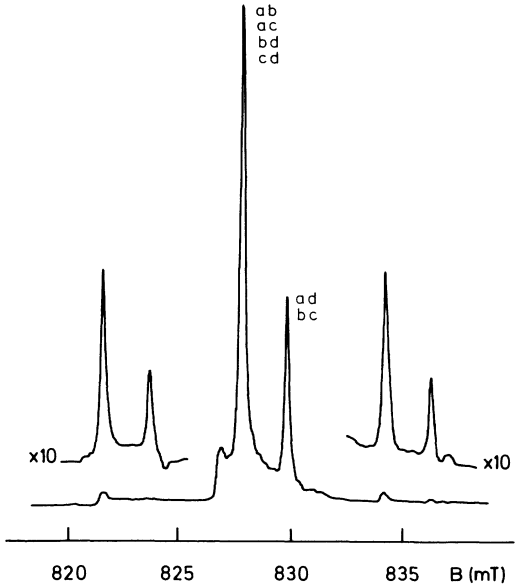

FIG. 3. EPR spectrum Si-G2 in dispersion mode with $\mathbf{B}\|[100]$ at a microwave frequency of 23.271 GHz. The orientation labels are indicated; clearly visible are the ^{29}Si hyperfine satellites due to the nearest-neighbor atoms a and d.

For the ENDOR measurements the experimental parameters were optimized for best signal-to-noise ratio. Lock-in detection of the EPR signal was done at a magnetic field modulation frequency of 83 Hz. The rf-induced changes in the EPR spectrum were monitored by

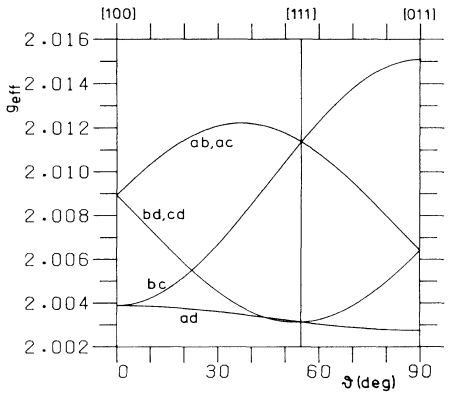

FIG. 4. Angular dependence of the effective g values of Si-G2 for rotation of the magnetic field in the $(0\bar{1}1)$ plane. Orientation labels are given.

a second lock-in detector which modulated the rf power on-off at a frequency of 3.3 Hz. The EPR lock-in was set to a time constant of 30 ms and its band-pass amplifier to a quality factor of 10 to allow the ENDOR signals to pass. The time constant of the ENDOR lock-in was adjusted to the scan speed of the rf in relation to the ENDOR linewidth, to achieve the best signal-to-noise ratio. Best results were achieved at low microwave power, typically 1 μW with a cavity quality factor $Q \simeq 7000$. The magnetic field was kept constant to within 2 μT by computer regulation. For the smaller hyperfine interactions the field was kept constant on the top of the EPR line, for the larger hyperfine interactions the field could be shifted automatically as a function of the rf frequency in order to keep the field locked on that part of the inhomogeneously broadened EPR line that contains the hyperfine satellites to be scanned. The rf frequency was swept slowly for typical slow-passage conditions. ENDOR linewidths ranged from 1.2 kHz for the smallest hyperfine interactions to 60 kHz for the largest: M*ad*1. This last interaction originates from the first-neighbor shell and is also seen in EPR. The optimum temperature for the ENDOR experiments was determined by measuring the ENDOR effect as a function of temperature for two specific ENDOR lines in the lower-frequency region. Figure 5 shows the results; also indicated are the EPR intensity and the phase angle of the EPR signal with respect to the magnetic field modulation. The temperature for the ENDOR experiments was thus set to ~ 18 K.

The curves of Fig. 5, and the fact that we use low microwave power, are an indication that partial saturation of the EPR signal, which is an alleged condition for good ENDOR results, is not the only optimal condition. Although spectrum Si-G2 saturates well below 15 K, the ENDOR yield has a rather sharp peak around 18 K. Figure 5 suggests that good ENDOR conditions are met when the phase of the EPR signal changes rapidly with temperature. Rather laborious experiments would have been necessary to unravel the processes involved.

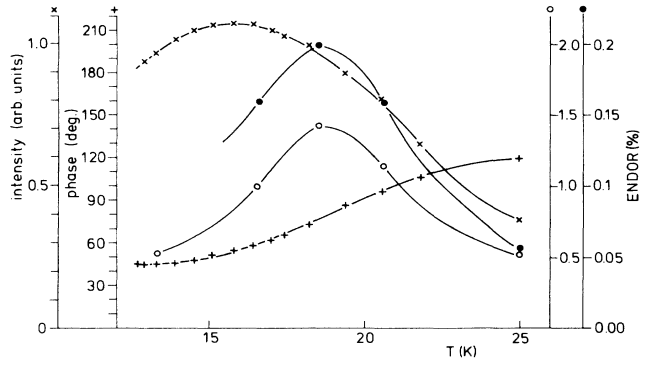

FIG. 5. EPR and ENDOR signal intensities as a function of temperature. $B = 827.87$ mT||[100], microwave frequency $\nu = 23.218$ GHz, vacancy orientations *ad*,*bc*. (×), intensity of the dispersion EPR signal in arbitrary units. (+), phase angle of the EPR signal with respect to the magnetic field modulation. (○), ENDOR effect, in percents of the EPR signal, for the ENDOR line at 7.1033 MHz, belonging to ENDOR shells M*ad*17 and G26. (●), ENDOR effect for the line at 7.572 MHz, of ENDOR shell M*ad*19.

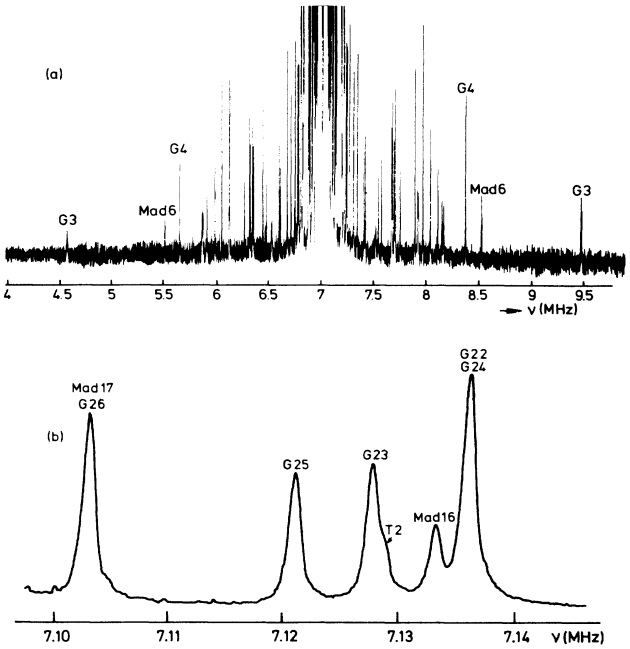

FIG. 6. ENDOR spectra for vacancy orientations *ad* and *bc*, $B = 827.87$ mT||[100]. Assignments of lines to hyperfine tensors are indicated. (a) Spectrum with low resolution showing the symmetry around the nuclear Zeeman frequency, 7.003 MHz. (b) Spectrum with a ~ 100 times higher resolution.

Examples of ENDOR spectra are given in Fig. 6. Figure 6(a) shows a broad scan at poor resolution to give a general picture. Here the symmetry around the nuclear Zeeman frequency is clearly visible. Figure 6(b) gives a specimen representative of the quality of the spectra used in the analysis of the lower part of the frequency range where ENDOR patterns often severely overlap.

D. Symmetry considerations for V^-

The EPR measurements of Si-G2 can be described with the spin Hamiltonian $\mathcal{H} = \mu_B \mathbf{B} \cdot \vec{\mathbf{g}} \cdot \mathbf{S}$. The $\vec{\mathbf{g}}$ tensor is determined by angular dependent measurements. The symmetry of the defect wave function follows from the symmetry of the $\vec{\mathbf{g}}$ tensor, which is that of point group $2mm$ in the case of V^-. This symmetry is consistent with the molecular-orbital treatment of Watkins. An energy-level scheme is given in Fig. 2. After the distortion from V^0 to V^-, the last electron is mainly concentrated on two of the four nearest-neighbor atoms. Figure 1(b) shows a model of V^- in one of its six possible orientations. The vacancy is at position [000]; the four nearest neighbors *a*, *b*, *c*, and *d* are at the positions $[\bar{1}11]$, $[11\bar{1}]$, $[1\bar{1}1]$, and $[\bar{1}\,\bar{1}\,\bar{1}]$, respectively. Orientations of V^- are labeled according to the pair of atoms on which the electron is concentrated after the final distortion. In Fig. 1(b) the vacancy is shown in orientation *ad*, which is our standard orientation wherever orientation-dependent information is given.

For this orientation the twofold symmetry axis of the vacancy is the [100] axis, and the two mirror planes are the $(0\bar{1}1)$ plane and the (011) plane. The constraints of invariance under the four operations of the point group $2mm$ (E,$m_{(0\bar{1}1)}$, $m_{(011)}$, and $2_{[100]}$) reduce the $\vec{\vec{g}}$ tensor to the form of $2mm$ symmetry.

When adding the interaction with one magnetic nucleus of ^{29}Si to the system, the symmetry is lowered. In the hyperfine interaction tensor (see Sec. I E) the symmetry of the vacancy, together with a magnetic nucleus on some neighbor position, is reflected. Starting at a neighbor position $[klm]$, the symmetry operations of the group $2mm$ give, in the most general case, four symmetry equivalent positions: $[klm]$, $[kml]$, $[k\,\bar{m}\,\bar{l}]$, and $[k\,\bar{l}\,\bar{m}]$. We call those four lattice positions an ENDOR shell. Hyperfine interactions of this triclinic type are labeled G.

For certain lattice positions the total symmetry of the system is higher than triclinic. When an atom is on one of the mirror planes of the vacancy, the resulting symmetry is of point group m. For atoms on the mirror plane of the atoms a and d, the hyperfine interactions are labeled Mad; for those on the mirror plane of the atoms b and c, Mbc. The pertaining ENDOR shells contain two symmetry equivalent positions. Due to the fact that the orientations ad and bc are separated in EPR, we can discriminate experimentally between hyperfine interactions of class Mad and of class Mbc. For atom positions on the twofold axis of the vacancy the symmetry of the system remains $2mm$. These hyperfine interactions are labeled T. There is only one atom per shell. Data on these four classes of atom positions around the negative vacancy are summarized in Table II.

E. Spin-Hamiltonian analysis

ENDOR measurements for a specific neighbor site are described with the spin Hamiltonian

$$\mathcal{H}=\mu_B \mathbf{B}\cdot\vec{\vec{g}}\cdot\mathbf{S}-g_N\mu_N\mathbf{B}\cdot\mathbf{I}+\mathbf{S}\cdot\vec{\vec{A}}\cdot\mathbf{I}\,, \tag{1}$$

where $S=\frac{1}{2}$, $I=\frac{1}{2}$, and $\vec{\vec{A}}$ is the hyperfine interaction tensor for that specific site. Generally, the parameters of this Hamiltonian were determined by a computer fit of the observed ENDOR frequencies to specific transitions, or differences between eigenvalues of the 4×4 Hamiltonian matrix. In order to unravel the sometimes complicated and severely overlapping ENDOR spectra, it is useful to have insight into the first-order solutions of this Hamiltonian. These are found as

$$E_{|m_S,m_I\rangle}=m_S g_{\mathrm{eff}}\mu_B B-m_I g_N\mu_N B+m_S m_I A_{\mathrm{eff}}\,, \tag{2}$$

with $m_S=\pm\frac{1}{2}$ and $m_I=\pm\frac{1}{2}$. EPR transitions are those with $\Delta m_S=\pm1$, $\Delta m_I=0$; NMR transitions are those with $\Delta m_S=0$, $\Delta m_I=\pm1$. This gives for the NMR, or ENDOR, frequencies

$$h\nu=\Delta E=|\,g_N\mu_N B\pm\tfrac{1}{2}A_{\mathrm{eff}}\,|\,, \tag{3}$$

where $g_{\mathrm{eff}}\mu_B B/h\simeq23$ GHz, $g_N\mu_N B/h\simeq7$ MHz (at $B\simeq0.8$ T), and $\frac{1}{2}A_{\mathrm{eff}}/h$ ranges from ~100 kHz to ~200 MHz. In order to sort out which ENDOR lines belong to which hyperfine tensor and to which orientation within a hyperfine shell, the values $|\,\nu-\nu_z\,|$, where $\nu_z=g_N\mu_N B/h$ is the nuclear Zeeman frequency, were roughly analyzed. At frequencies $\nu>\nu_z$ this quantity is, except for the larger interactions, equal to $\frac{1}{2}A_{\mathrm{eff}}/h$. In most cases only these transitions were used. In computer fits for the hyperfine tensors the electronic g values were kept constant to those found in a fit of the EPR spectrum. For one specific hyperfine tensor, points from both ENDOR transitions were used simultaneously which allowed a fit of the nuclear g value. We found $|\,g_N\,|=1.1097\pm0.0001$, in close agreement with values in nuclear tables.[17] For all other fits the nuclear g value was kept constant to this value. For values of $\nu-\nu_z>3$ MHz, the angular patterns of the different hyperfine tensors hardly overlap and the assignment was rather easy. In the lower-frequency region, however, ENDOR patterns of different hyperfine tensors exhibit severe overlap. This overlap, together with the linewidth, sets the limit for the smallest hyperfine tensor that can be resolved. In order to do the sorting in this region close to ν_z, values of $\nu-\nu_z$, or $\frac{1}{2}A_{\mathrm{eff}}$, were plotted as a function of the angle in the $(0\bar{1}1)$ plane for the orientations ad and bc. The angular dependence was plotted with 10° or 5° intervals, or in some regions even with 2° intervals. For the two orientations ad and bc, at most angles the EPR lines are separated well enough from each other and from those of the other four orientations to avoid confusion (see Fig. 4). With the aid of the rules given in Ref. 18, the class could be determined. For magnetic fields in the $(0\bar{1}1)$ plane the ENDOR lines from atoms at symmetric positions with respect to this plane coincide two by two for orientations ad and bc. As a result, each of them gives two ENDOR lines in the case of a general-class tensor. Orientation ad gives two lines and

TABLE II. Properties of the different types of hyperfine tensors and associated shells for the vacancy V^-. N_{at} is the number of atoms per shell; atom positions refer to orientation ad. Constraints on the general symmetric form of the hyperfine tensor $\vec{\vec{A}}$ are given. The number of ENDOR lines is indicated for the three high-symmetry directions in the $(0\bar{1}1)$ plane.

Class	Symmetry	N_{at}	Positions	Constraints	No. of lines, **B**|| [100]	[111]	[011]
T	$2mm$	1	[100] axis	$A_{yy}=A_{zz};A_{xy}=A_{xz}=0$	2	2	3
Mad	m	2	$(0\bar{1}1)$ plane	$A_{yy}=A_{zz};A_{xy}=A_{xz}$	2	3	4
Mbc	m	2	(011) plane	$A_{yy}=A_{zz};A_{xy}=-A_{xz}$	2	3	4
G	1	4	Others		3	4	6

bc only one in the case of an M*ad*-class tensor; *ad* gives one and *bc* two for an M*bc* tensor. Both *ad* and *bc* give only one ENDOR line for a T-class tensor. Once a set of curves from the orientations *ad* and *bc* was decided as belonging to one tensor, the points of the other four orientations (*ab*, *ac*, *bd*, and *cd*) were predicted and afterwards verified. In cases of ambiguity due to nearly overlapping lines, computer fits gave the solution. Fits were accepted if all observed points were fitted within the ENDOR linewidth. In most cases only the slowly scanned lines in the high-symmetry directions [100], [111], and [011] were used for the fits.

Computer fits were made using a least-squares minimization method. For this purpose transition frequencies are calculated as a function of the Hamiltonian parameters and of experimental quantities such as the magnetic field vector and the defect orientation. A general-purpose FORTRAN library, named EPRLIB, performs the fitting of the Hamiltonian parameters.[19]

F. Linear combination of atomic orbitals analysis

The interaction between the electronic spin **S** and the nuclear spin **I** can be represented quantum mechanically by a dipole-dipole interaction operator. The hyperfine interaction tensor follows from integration of this operator over the spatial part of the electronic wave function. The hyperfine tensor can be decomposed into an isotropic and a traceless part:

$$\overleftrightarrow{A}=a\overleftrightarrow{1}+\overleftrightarrow{B} . \tag{4}$$

The isotropic part is the Fermi-contact interaction which is proportional to the density of the electronic wave function at the site r_0 of the nucleus:

$$a=\tfrac{2}{3}\mu_0 g\mu_B g_N\mu_N \mid \Psi(r_0)\mid^2 , \tag{5}$$

where Ψ is the electronic wave function. The anisotropic tensor $\overleftrightarrow{B}$ describes the classical dipole-dipole interaction and can be written

$$B_{ij}=\frac{\mu_0}{4\pi}g\mu_B g_N\mu_N\left\langle\Psi\left|\frac{3x_ix_j}{r^5}-\frac{\delta_{ij}}{r^3}\right|\Psi\right\rangle , \tag{6}$$

where $x_i,x_j=x,y,z$.

Electronic wave functions of defects in silicon are often described as linear combinations of atomic orbitals (LCAO). A one-electron wave function is then written as

$$\Psi=\sum_i \eta_i\phi_i , \tag{7}$$

where i enumerates lattice sites and the contributions ϕ_i on these sites are hybrid combinations of silicon $3s$ and $3p$ orbitals:

$$\phi_i(\mathbf{r})=\alpha_i\psi_s(\mathbf{r})+\beta_i\psi_p(\mathbf{r}) . \tag{8}$$

Substitution of Eqs. (7) and (8) into Eqs. (5) and (6) yields for the Fermi-contact interaction

$$a_i=\tfrac{2}{3}\mu_0 g\mu_B g_N\mu_N\eta_i^2\alpha_i^2 \mid \psi_s(0)\mid^2 , \tag{9}$$

under the assumption that ψ_s and ψ_p decrease sufficiently fast with the distance **r**, that at site i only the contribution from orbitals centered on atom i itself has to be taken into account. Under the same assumption, the anisotropic interaction gives an axial hyperfine tensor $\overleftrightarrow{B}_i$ with principal values $(2b_i,-b_i,-b_i)$, whose axial direction is the direction of the p lobe and where b_i has the value

$$b_i=\frac{\mu_0}{4\pi}g\mu_B g_N\mu_N\eta_i^2\beta_i^2\tfrac{2}{5}\langle r^{-3}\rangle_p . \tag{10}$$

The quantities $\mid\psi_s(0)\mid^2$ and $\langle r^{-3}\rangle_p=\langle\psi_p\mid r^{-3}\mid\psi_p\rangle$ are constants from the atomic wave functions and independent of the specific defect or molecule. When they are known, the s-character fraction α_i^2, the p-character fraction β_i^2, and the degree of localization η_i^2 of the paramagnetic electron on the atomic site i can be determined. In the analysis of our ENDOR results we will use values given by Morton and Preston,[20] calculated by numerical integration of the wave functions of Herman and Skillman:[21] $\mid\psi_s(0)\mid^2=34.6\times10^{30}$ m^{-3} and $\langle r^{-3}\rangle_p=18.2\times10^{30}$ m^{-3}. These values are $\sim10\%$ higher than the values introduced by Watkins and Corbett in 1964.[22] It is clear that this analysis is only fully valid in the case of axial hyperfine tensors, because of the axial character of the p orbitals. Moreover, a_i and b_i must have the same sign.

II. EXPERIMENTAL RESULTS

A. Hyperfine tensors

From the measurements, the absolute sign of the hyperfine tensors cannot be determined. Therefore for all tensors the isotropic part, $a=\frac{1}{3}\mathrm{Tr}(\overleftrightarrow{A})$, is given as a positive value. Subsequently, the tensors are ordered with decreasing a values within each symmetry class. A total number of 51 hyperfine tensors is found, 26 of which are of the general class (G1—G26), 18 of the mirror-plane class M*ad* (M*ad* 1—M*ad* 18), 5 of the mirror-plane class M*bc* (M*bc* 1—M*bc* 5), and 2 of the twofold axis class (T1 and T2). The total number of atoms covered by these measurements is thus 152. The total number of independent tensor parameters is 254. These experimental results are given in Table III. Data always refer to one of the atoms of a shell belonging to EPR orientation *ad*. Given are the principal values and principal directions of the tensors. A more detailed presentation of the data, together with a graphical representation of the hyperfine tensors, is given in Ref. 8. Some representative plots of hyperfine interactions from all symmetry classes are shown in Fig. 7.

B. LCAO parameters

New parameters a, b, and c were derived from the principal values by equating these values to $a+2b$, $a-b+c$, and $a-b-c$. a is the isotropic part of the hyperfine interaction, b is the parameter determining the symmetric axial traceless tensor $\overleftrightarrow{B}$ with principal values $+2b$, $-b$, and $-b$, and c is the deviation from axial symmetry. b and c are chosen such that $\mid b\mid>\mid c\mid$. This implies that sometimes $b<0$; in those cases, $A_3=a+2b$; otherwise, $A_1=a+2b$.

As discussed in Sec. I F, a and b can be related to the

TABLE III. Hyperfine parameters of the negatively charged vacancy. Principal values A_i are given in kHz. γ_i is the angle of the ith principal direction with the $(0\bar{1}1)$ plane; δ_i is the angle between the projection of this direction on the $(0\bar{1}1)$ plane and the [100] direction. These figures refer to EPR orientation *ad*. Experimental errors range from 4 kHz for M*ad* 1 to 0.1 kHz for most smaller interactions.

Tensor	A_1	A_2	A_3	γ_1	δ_1	γ_2	δ_2	γ_3	δ_3
G1	17444.7	11391.2	11262.3	−1.2	57.1	−31.8	−33.7	58.1	−31.0
G2	11044.5	6513.1	6347.1	−1.4	60.4	−46.2	−31.1	43.7	−28.3
G3	6060.2	4284.8	4186.7	−52.4	−1.2	31.0	37.7	19.2	−64.4
G4	3044.2	2736.5	2335.5	−62.2	19.5	27.7	22.0	1.0	−68.5
G5	2312.1	2006.8	1866.8	−67.3	−86.0	−15.9	46.8	15.8	−38.5
G6	2584.6	1762.2	1717.2	−2.5	52.0	28.8	−36.6	−61.0	−42.6
G7	3068.8	2409.1	540.2	−40.3	−75.1	−19.7	32.6	43.2	−37.7
G8	1958.7	1794.9	1501.8	−47.3	31.8	42.6	26.8	−2.5	−60.9
G9	1992.3	1107.0	1073.2	−1.3	58.9	51.6	−29.4	−38.4	−32.1
G10	1753.1	1202.3	1188.6	−53.3	2.6	31.9	36.2	16.3	−64.2
G11	1886.3	1131.8	1120.9	−2.4	57.6	−46.1	−34.9	43.8	−30.1
G12	748.8	666.8	519.8	−54.3	30.0	34.9	16.0	−6.6	−69.3
G13	834.3	530.3	489.6	56.8	88.5	−16.4	25.2	28.0	−55.8
G14	740.4	443.5	440.1	−7.2	42.8	−51.5	−56.2	37.6	−41.6
G15	567.1	405.3	392.8	−4.5	49.9	29.5	−37.6	−60.1	−48.0
G16	568.6	386.3	368.2	−60.7	22.0	1.8	−64.8	29.2	26.1
G17	571.3	368.7	367.4	−49.3	6.1	21.6	−56.6	32.6	48.1
G18	502.3	352.8	351.5	−52.8	1.6	25.7	52.2	24.9	−50.8
G19	535.2	311.2	304.8	−1.8	62.3	−51.2	−30.0	38.7	−26.3
G20	414.6	351.6	286.0	−15.5	7.3	2.6	−82.0	74.3	17.5
G21	386.7	353.4	252.8	−49.4	20.0	40.0	8.5	−5.7	−76.7
G22	451.0	270.0	246.5	−61.3	61.2	−13.3	−54.4	24.9	29.3
G23	326.6	295.3	189.6	−8.0	85.8	−41.0	−11.3	47.9	4.7
G24	364.6	217.5	208.7	−1.6	55.5	−2.1	−34.6	87.3	2.6
G25	353.7	205.4	204.9	−1.3	63.5	−67.9	−29.7	22.0	−26.0
G26	312.7	206.7	198.6	−46.1	86.2	−43.0	−79.0	7.4	4.0
M*ad* 1	400452.4	334805.1	332279.4	0.0	54.8	90.0		0.0	−35.2
M*ad* 2	61182.1	45376.5	44051.1	0.0	55.0	90.0		0.0	−35.0
M*ad* 3	37859.1	27143.2	26561.1	0.0	53.0	90.0		0.0	−37.0
M*ad* 4	16447.3	12131.9	11824.2	0.0	55.2	90.0		0.0	−34.8
M*ad* 5	7803.6	5639.3	5514.2	0.0	55.9	90.0		0.0	−34.1
M*ad* 6	3799.1	2746.5	2683.9	0.0	55.7	90.0		0.0	−34.3
M*ad* 7	3246.4	1959.8	1918.0	0.0	58.2	0.0	−31.8	90.0	
M*ad* 8	1855.8	1366.9	1338.1	0.0	56.9	90.0		0.0	−33.1
M*ad* 9	1338.2	1221.5	991.3	90.0		0.0	37.1	0.0	−52.9
M*ad* 10	1394.2	952.3	869.5	0.0	10.6	0.0	−79.4	90.0	
M*ad* 11	1505.2	843.9	840.3	0.0	54.1	0.0	−35.9	90.0	
M*ad* 12	994.5	728.4	715.3	0.0	56.5	90.0		0.0	−33.5
M*ad* 13	546.2	291.0	285.2	0.0	54.9	0.0	−35.1	90.0	
M*ad* 14	457.9	333.2	327.8	0.0	58.1	90.0		0.0	−31.9
M*ad* 15	536.6	288.9	288.7	0.0	56.3	90.0		0.0	−33.7
M*ad* 16	333.4	323.7	212.8	90.0		0.0	−49.8	0.0	40.2
M*ad* 17	250.0	182.2	179.1	0.0	58.1	90.0		0.0	−31.9
M*ad* 18	390.5	20.0	−42.6	0.0	81.2	0.0	−8.8	90.0	
M*bc* 1	2458.3	2026.4	1832.6	−31.1	0.0	0.0	90.0	58.9	0.0
M*bc* 2	2406.2	1968.9	1617.6	−41.6	0.0	48.4	0.0	0.0	90.0
M*bc* 3	965.3	798.9	727.3	−66.9	0.0	23.1	0.0	0.0	90.0
M*bc* 4	249.4	233.7	145.9	0.0	90.0	−49.1	0.0	40.9	0.0
M*bc* 5	1564.7	−402.3	−551.1	−31.3	0.0	0.0	90.0	58.7	0.0
T1	772.5	708.0	518.0	90.0		0.0	90.0	0.0	0.0
T2	348.0	250.6	249.4	90.0		0.0	0.0	0.0	90.0

TABLE IV. Reduced hyperfine parameters and calculated LCAO parameters of the vacancy. Values of a, b, and c are in units of kHz. s-character fractions α^2, p-character fractions β^2, and localization η^2 are calculated with the atomic wave-function parameters from Ref. 20, taking the absolute values of a and b. The suitability of the LCAO description is indicated by + or −. Assignment to lattice positions according to various model descriptions is given (see text).

Tensor	a	b	c	a/b	b/c	α^2	β^2	η^2(%)	LCAO	Position	Model
G1	13 366.0	2039.3	64.4	6.55	31.65	0.140	0.860	2.08	+	[$\bar{2}$24]	ch2
G2	7968.2	1538.2	83.0	5.18	18.53	0.114	0.886	1.52	+		
G3	4843.9	608.1	49.0	7.97	12.41	0.165	0.835	0.64	+	[$\bar{3}$35]	ch2
G4	2705.4	−184.9	−153.8	−14.63	1.20	0.267	0.733	0.22	−		
G5	2061.9	125.1	70.0	16.48	1.79	0.291	0.709	0.15	−		
G6	2021.3	281.6	22.5	7.18	12.52	0.151	0.849	0.29	+	[$\bar{4}$26]	ch2
G7	2006.1	−732.9	−329.8	−2.74	2.22	0.064	0.936	0.69	−		
G8	1751.8	−125.0	−81.9	−14.01	1.53	0.258	0.742	0.15	−		
G9	1390.8	300.7	16.9	4.62	17.78	0.103	0.897	0.29	+		
G10	1381.3	185.9	6.9	7.43	27.01	0.156	0.844	0.19	+	[$\bar{5}$37]	ch2
G11	1379.7	253.3	5.4	5.45	46.56	0.119	0.881	0.25	+		
G12	645.2	−62.7	−41.0	−10.30	1.53	0.204	0.796	0.07	−		
G13	618.0	108.1	20.4	5.72	5.31	0.124	0.876	0.11	+		
G14	541.3	99.5	1.7	5.44	59.74	0.119	0.881	0.10	+		
G15	455.1	56.0	6.2	8.13	9.02	0.168	0.832	0.06	+	[$\bar{6}$28]	ch2
G16	441.0	63.8	9.1	6.91	7.03	0.147	0.853	0.07	+		
G17	435.8	67.8	0.6	6.43	108.51	0.138	0.862	0.07	+		
G18	402.2	50.1	0.7	8.03	76.44	0.166	0.834	0.05	+		
G19	383.7	75.7	3.2	5.07	23.79	0.112	0.888	0.07	+		
G20	350.7	−32.4	−31.5	−10.83	1.03	0.212	0.788	0.04	−		
G21	331.0	−39.1	−16.6	−8.47	2.35	0.174	0.826	0.04	−		
G22	322.5	64.2	11.7	5.02	5.48	0.111	0.889	0.06	+	[004]	dd
G23	270.5	−40.5	−15.6	−6.69	2.59	0.143	0.857	0.04	−		
G24	263.6	50.5	4.4	5.22	11.47	0.115	0.885	0.05	+		
G25	254.7	49.5	0.2	5.14	203.06	0.113	0.887	0.05	+		
G26	239.3	36.7	4.0	6.53	9.08	0.140	0.860	0.04	+	[$\bar{1}$15]	dd
Mad 1	355 845.6	22 303.4	1262.9	15.95	17.66	0.284	0.716	27.28	+	[$\bar{1}$11]	ch
Mad 2	50 203.2	5489.4	662.7	9.15	8.28	0.185	0.815	5.90	+	[022]	ch
Mad 3	30 521.1	3669.0	291.1	8.32	12.61	0.171	0.829	3.88	+	[$\bar{1}$33]	ch
Mad 4	13 467.8	1489.7	153.9	9.04	9.68	0.183	0.817	1.60	+	[044]	ch
Mad 5	6319.0	742.3	62.6	8.51	11.87	0.175	0.825	0.79	+	[$\bar{1}$55]	ch
Mad 6	3076.5	361.3	31.3	8.52	11.56	0.175	0.825	0.38	+	[066]	ch
Mad 7	2374.7	435.8	20.9	5.45	20.89	0.119	0.881	0.43	+		
Mad 8	1520.3	167.8	14.4	9.06	11.65	0.184	0.816	0.18	+	[$\bar{1}$77]	ch
Mad 9	1183.7	−96.2	−58.4	−12.31	1.65	0.234	0.766	0.11	−		
Mad 10	1072.0	161.1	41.4	6.65	3.89	0.142	0.858	0.16	−		
Mad 11	1063.1	221.0	1.8	4.81	123.42	0.107	0.893	0.22	+		
Mad 12	812.7	90.9	6.6	8.94	13.88	0.182	0.818	0.10	+	[088]	ch
Mad 13	374.1	86.0	2.9	4.35	29.74	0.098	0.902	0.08	+		
Mad 14	373.0	42.5	2.7	8.78	15.81	0.179	0.821	0.05	+	[$\bar{1}$99]	ch
Mad 15	371.4	82.6	0.1	4.50	753.80	0.101	0.899	0.08	+		
Mad 16	290.0	−38.6	−4.9	−7.52	7.87	0.157	0.843	0.04	−		
Mad 17	203.7	23.1	1.5	8.80	14.95	0.180	0.820	0.02	+	[0 10 10]	ch
Mad 18	122.6	134.0	31.3	.92	4.28	0.022	0.978	0.12	−		
Mbc 1	2105.8	176.3	96.9	11.95	1.82	0.229	0.771	0.20	−	[$\bar{3}\bar{1}$1]	dd
Mbc 2	1997.6	204.3	175.7	9.78	1.16	0.196	0.804	0.22	−		
Mbc 3	830.5	67.4	35.8	12.32	1.88	0.234	0.766	0.08	−		
Mbc 4	209.6	−31.9	−7.8	−6.57	4.07	0.140	0.860	0.03	−		
Mbc 5	203.8	680.5	74.4	0.30	9.14	0.007	0.993	0.60	+	[1$\bar{1}$1]	dd
T1	666.2	−74.1	−32.3	−8.99	2.30	0.183	0.817	0.08	−	[$\bar{4}$00]	dd
T2	282.7	32.7	0.6	8.65	52.66	0.177	0.823	0.03	+	[400]	dd

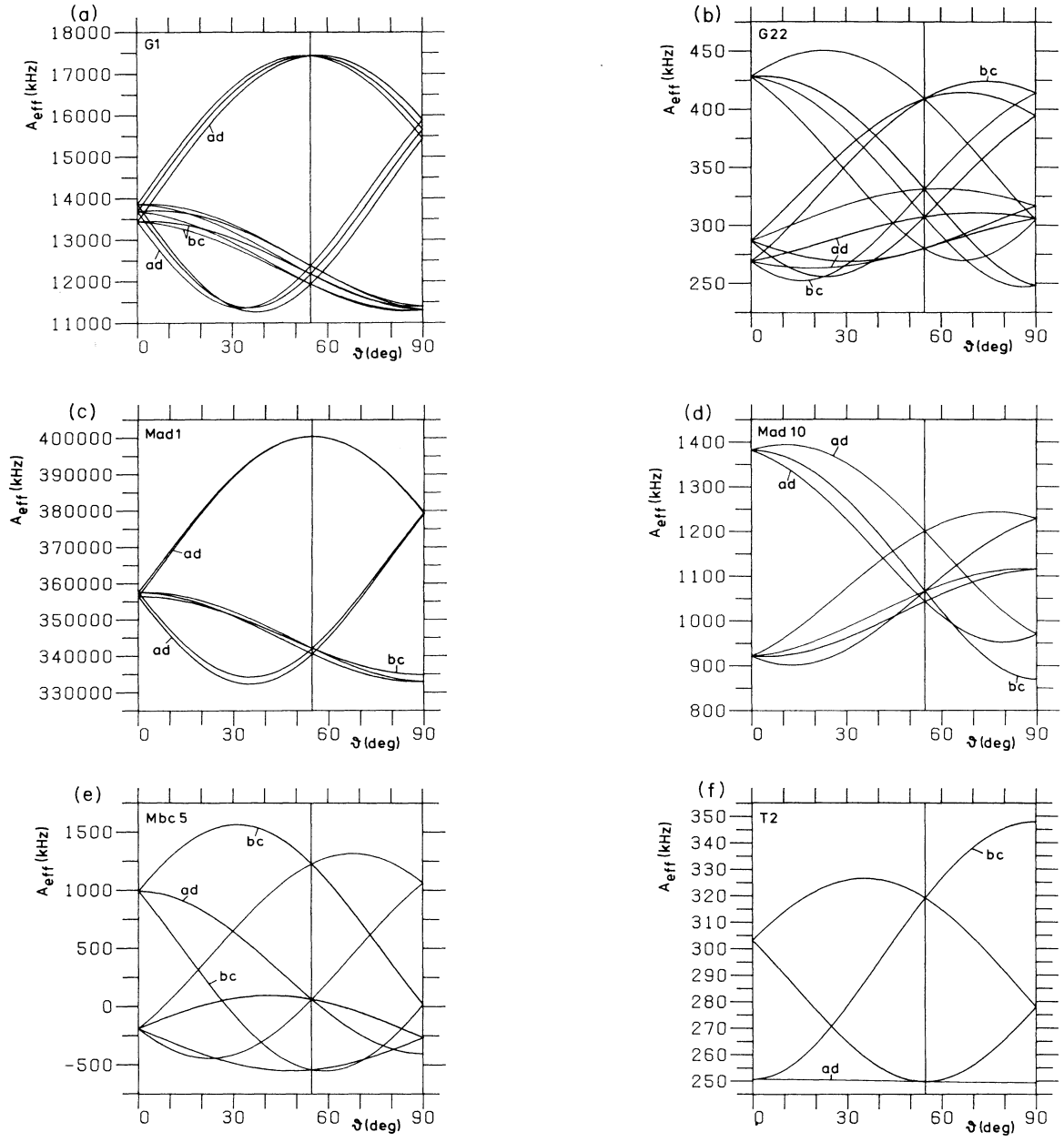

FIG. 7. Angular dependent patterns of effective hyperfine interactions A_{eff} from all four classes of neighbor shells. Plots have been calculated with the fitted values from Table III, for a magnetic field in the $(0\bar{1}1)$ plane. Lines from orientations *ad* and *bc* for which the $(0\bar{1}1)$ plane is a symmetry plane are explicitly indicated. (a) Tensor G1 which is nearly $\langle 111 \rangle$ axial. (b) Tensor G22 which is not axial at all. (c) Tensor M*ad* 1, nearly $\langle 111 \rangle$ axial and identified with the nearest-neighbor atoms. (d) Tensor M*ad* 10 which is nearly $\langle 100 \rangle$ axial. (e) Tensor M*bc* 5 which crosses $A_{\text{eff}}=0$ as a result of its large anisotropy. (f) Tensor T2 which is almost $\langle 011 \rangle$ axial.

defect wave function. As absolute signs of the interactions are not experimentally known, a is given as positive for all tensors only for simplicity. Although it is known that g_N is actually negative, positive LCAO parameters α^2, β^2, and η^2 have been derived from these values. Results for the 51 vacancy shells are given in Table IV. This analysis is not without problems, as any LCAO description with $3s$ and $3p$ atomic orbitals yields purely axial hyperfine tensors. Taking $|b/c| > 5$ as a rather arbitrary criterion for axiality, we find that 16 of the 51 hyperfine tensors are to be considered nonaxial. Another problem occurs when a and b have different signs, which is the case for 11 tensors. Ten of those belong to the nonaxial tensors, so that for 17 tensors an LCAO analysis is not suitable.

Multiplication of the η^2 values with the number of

atoms per shell and summation gives a total localization of 114.8%. 82.8% of it is in the *ad* plane, 29.6% on general class atoms, 2.3% on the *bc* plane, and 0.1% on the two T sites. If the above-mentioned 17 tensors are not included, still a total of 105.1% is left. This is another indication that a LCAO description of hyperfine interactions is not fully adequate. Some reasons will be discussed in the next section.

III. DISCUSSION

A. Localization in the *ad* plane

The data presented in the preceding section provide detailed information on the wave function of the defect electron of the negatively charged vacancy over a region of 152 atom positions. However, the interpretation of the data in terms of defect-wave-function parameters is not always possible in an unambiguous way. A first step should be an assignment of hyperfine tensors to shells of lattice sites. Part of this assignment follows directly from the division of the tensors into the four symmetry classes as given in Tables III and IV. Here we take advantage of the relatively high symmetry of the defect, giving four classes, in contrast to, e.g., the divacancy in silicon, which has only two,[12,13] or the boron-vacancy complex, which has only one class.[8,23] However, the experiment does not give any direct clue to the assignment of tensors to shells within the symmetry classes. As theoretical calculations are beyond the scope of this work, we will restrict ourselves to an interpretation of the data from phenomenological points of view.

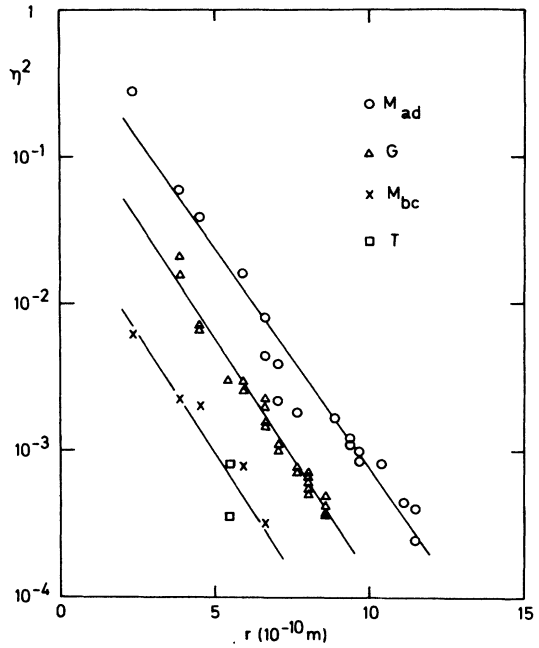

FIG. 8. Hyperfine interactions of V^- converted to values for the localization of the wave function, plotted against the distance from the vacancy under the assumption of monotonic decrease. Solid lines are fitted to the functions $\eta(r)^2 = \eta_0^2 \exp(-r/r_0)$ for tensor classes G, M*ad*, and M*bc* + T, respectively.

TABLE V. Parameters for the fitted curves of Fig. 8. For comparison, similar values for both charge states of the divacancy are included (Refs. 12 and 13).

Defect	Shell type	η_0^2	r_0 (Å)
V^-	G	0.23	1.4
V^-	M*ad*	0.72	1.5
V^-	M*bc* + T	0.04	1.4
VV^-	G	0.61	1.1
VV^-	M	0.83	1.3
VV^+	G	0.35	1.1
VV^+	M	17.15	0.7

As was already shown in Sec. II B, the defect wave function is highly localized in the plane of the vacancy and the atoms *a* and *d*. The LCAO analysis finds 83% of the unpaired electron in this plane, against only 2.3% on the plane of the atoms *b* and *c*. In previous work we calculated the probability density of the electron from the values of the contact interactions a_i for only 27 shells of atoms.[24] Values of $|\Psi(r_i)|^2$ were plotted against distance, assuming monotonic decrease within the symmetry classes. A similar result is found when the values for η^2 from Table IV are plotted for all 51 hyperfine shells of the vacancy, as shown in Fig. 8. Per symmetry class (M*bc* and T taken together), the experimental points are fitted to the curves $\eta(r)^2 = \eta_0^2 \exp(-r/r_0)$. The parameters are given in Table V. The resulting picture of the wave function is only very crude because of the assumption of monotonic decrease. From the large differences between the symmetry classes it is already clear that the wave function as a whole is not decreasing monotonically with distance. The analysis can help, however, in making a comparison with other ENDOR data, e.g., from the divacancy in silicon, for which data are also included in Table V.[12,13] The extent of the wave function (parameter r_0) of V^- is seen to be comparable to that of VV^-, whereas the wave function of VV^+ is slightly more localized.

B. The vacancy as a one-dimensional defect

In this section the distribution of the defect wave function within the $(0\bar{1}1)$ plane of the atoms *a* and *d* is considered in more detail. Firstly, we assume that the largest M*ad* shell, M*ad* 1, arises from the nearest-neighbor atoms of the vacancy, the atoms *a* and *d*. The one-electron LCAO model (Fig. 2) predicts the unpaired electron in an *a*-*d* molecular orbital, which gives large probability densities on the atoms *a* and *d*.[2,3] Having made this assignment, 55% of the unpaired electron is found on these two atoms. It is tempting to argue that the next-largest hyperfine tensors of symmetry type M*ad* arise from the atoms on the neighbor shells connected to the nearest neighbors

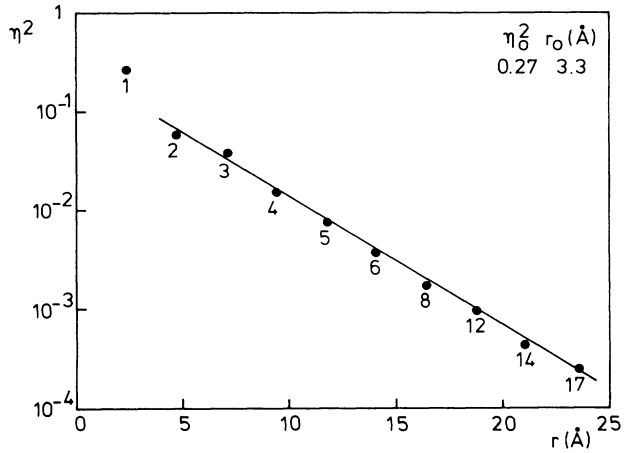

FIG. 9. The localization η^2 of the wave function of V^- as a function of the distance to the vacancy site, taken along the [011] chain. The numbers at the points indicate the M*ad* tensors. The line is a logarithmic fit to the curve $\eta(r)^2=\eta_0^2\exp(-r/r_0)$ for which parameters are given. Tensor M*ad* 1 is not included in the fit.

by ⟨111⟩ bonds in the M*ad* plane. This seems not unreasonable in a covalent solid, where the directed atom-atom bonds play a dominant role in the constitution of the lattice. Such a picture suggests a defect where the wave function mainly runs out along the zig-zag chains of atoms along the [011] direction. This suggestion has been made before.[24–26] The situation here is especially comparable with the Si-B1 center, the negative charge state of the oxygen-vacancy complex.[25]

Careful inspection of Tables III and IV and of angular plots of the hyperfine interactions reveals that tensors

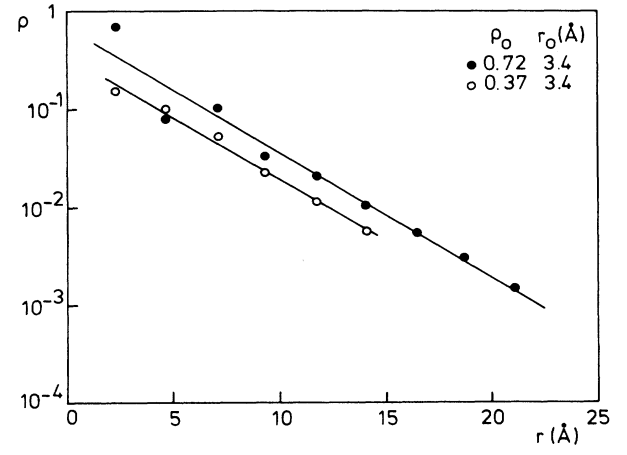

FIG. 10. Calculated charge density ρ, in units of an electron charge, taken from Ref. 28, for the atom positions on coplanar ⟨110⟩ chains around an impurity in silicon, as a function of the distance to the impurity site. (●), bound-state shell charge for a bound state at $E_b=0.6$ eV above the valence-band edge (Table III in Ref. 28). (○), total charge for $E_b=0.4$ eV (Table IV in Ref. 28). The lines are fits to the curves $\rho(r)=\rho_0\exp(-r/r_0)$ for which parameters are given.

M*ad* 1—M*ad* 6 are all very similar, except for their absolute magnitude. Similar to these are also M*ad* 8, M*ad* 12, M*ad* 14, and M*ad* 17. This similarity of tensors and consequently of angular dependent patterns manifests itself in the fact that (i) they are all very nearly [111] axial, (ii) their second axes are all perpendicular to the plane, and (iii) their ratios a/b and b/c have about the same values, except for M*ad* 1, which is slightly different. The somewhat exceptional position of M*ad* 1 is not unreasonable, as M*ad* 1 arises from the first neighbors of the vacancy in a region where substantial distortions are expected to occur. In Fig. 9 the values of the localization η^2 are plotted against the distance along a ⟨011⟩ chain. All of these ten points, except for the first, fall on an excellent straight line, indicating exponential decrease.

In this model a picture arises of a pseudo-one-dimensional defect whose atoms lie on a zig-zag line around [011]. The extension of the wave function along the chain is very large because of the low dimensionality: the lattice shell which gives rise to hyperfine tensor M*ad* 17 in this model, lies at a straight distance of 19.2 Å from the vacancy. Assignment of these chain shells is indicated in Table IV by ch. Following the LCAO analysis, 80% of the wave function can be found on this linear chain, an amount large enough to check with theoretical methods. The exponentially decreasing wave function is consistent with a theoretical Green's-function treatment in one dimension, with a very localized potential;[27] M*ad* 1 differs because it is associated with atoms within the range of the potential.

Very recently, in theoretical work by Kane,[28] these ideas about concentration of the defect electron on ⟨110⟩ coplanar atom chains have been strongly supported. A calculation is presented concerning the charge disturbance around a substitutional, singly negatively charged impurity of unspecified nature in a Green's-function treatment. The charge density is calculated for up to 72 shells of lattice sites surrounding the impurity. The most striking feature is the strong preference with which the charge concentrates on the coplanar ⟨110⟩ chains of atoms, of which 12 exist in cubic symmetry. In Fig. 10 we plot a small part of Kane's results in a manner comparable to our experimental results in Fig. 9. Especially at larger distances from the impurity site the decrease of the charge density is exponential, with a decay length r_0 of the same value as that for our vacancy results. Although in our experiment the symmetry is different, with only 2 of the 12 possible ⟨110⟩ chains, i.e., the [011] and [0$\bar{1}\bar{1}$] chains, the feature of charge concentration on very specific lattice chains is strongly supported.

Returning to the present vacancy study, one can try to discover more such series in the experimental data. Among the general-class tensors the numbers G1, G3, G6, G10, and G15 show similarities in a similar way as the M*ad* chain tensors. They are all ⟨111⟩ axial, alternating between the direction of the a or d bonds and the b or c bonds of the vacancy. Their second axes are again perpendicular to a {110} plane. The decrease is exponential with a comparable decay length (roughly a factor of 2 between adjacent chain sites). The location of this chain in the lattice poses some more problems. If the second hy-

perfine axes are supposed to be perpendicular to the plane in which the chain lies (as in the case of the M*ad* chain) then the direction of the chain should be [10$\bar{1}$], [1$\bar{1}$0], [110], or [101]. For symmetry reasons one cannot discriminate between these four directions. Of course, one is tempted to locate the starting point of this chain (tensor G1) at the nearest general-class atom site of the vacancy, the [$\bar{2}$02] lattice position. Another position, however, seems a better candidate for the location of tensor G1: the [$\bar{2}$24] lattice site. Justification for this choice is the striking similarity, also in magnitude, between the hyperfine tensors M*ad*4 and G1. This suggests that the G-class chain branches off from the M*ad* chain at [$\bar{1}$33], where tensor M*ad*3 is located. In that case the lattice positions for this side chain are G1[$\bar{2}$24], G3[$\bar{3}$35], G6[$\bar{4}$26], G10[$\bar{5}$37], and G15[$\bar{6}$28]. These identifications (marked ch2 in Table IV) are of course extremely tentative and are given as a challenge to theoretical calculations.

C. The forbidden plane

The level scheme of Watkins's molecular orbital model for the case of V^- (Refs. 2 and 3) is shown in Fig. 11. One-electron wave functions of this four-level system, in terms of the dangling-bond orbitals a, b, c, and d, are

$$a_1' = \frac{(b+c)+\lambda(a+d)}{(1+\lambda^2)^{1/2}} , \tag{11a}$$

$$a_1'' = \frac{\lambda(b+c)-(a+d)}{(1+\lambda^2)^{1/2}} , \tag{11b}$$

$$b_1 = a-d , \tag{11c}$$

$$b_2 = b-c . \tag{11d}$$

In the ground state in which the hyperfine interaction is observed, the unpaired electron has a b_1-type wave function. This wave function is antisymmetric with respect to the plane of atoms b and c, the (011) plane. This implies a vanishing electron density, and hence zero contact hyperfine interaction for atom positions on the plane. In Sec. III A we showed that the electron density in this plane is indeed more than an order of magnitude smaller than on the *ad* plane, confirming the symmetry assignment. However, from Tables III and IV it can be seen that the contact terms do not really vanish for class M*bc* and T tensors. For the largest, M*bc*1, $a = 2.1$ MHz which is indeed small compared to the value for M*ad*1 (356 MHz), but not negligible.

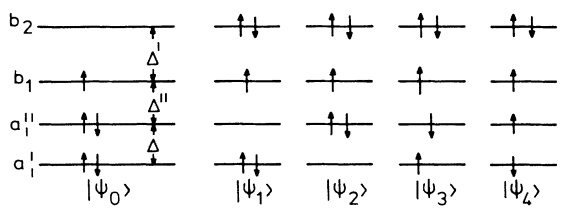

FIG. 11. Energy levels of V^- in the one-electron molecular orbital approach. Besides the ground state $|\psi_0\rangle$, also the four excited states with B_1 symmetry, $|\psi_1\rangle$ to $|\psi_4\rangle$, are shown.

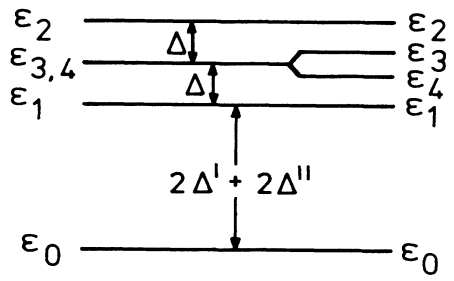

FIG. 12. Many-electron energy levels of V^-. Levels ε_3 and ε_4 are degenerate to first order. Spin-spin interaction splits these levels.

One might of course argue that the order of the levels is different from that given in Figs. 2 and 11, the a_1'' level being above the b_1 level, allowing electron density on the *bc* plane.[24] As this would require an unrealistically large energy for the additional distortion compared to the tetragonal, this explanation seems rather improbable.[29] Moreover, this would have led to larger and better axial hyperfine interactions than experimentally observed.

A better explanation is found in the fact that the one-electron description itself may not be fully adequate, as more-electron effects have to be considered. When remaining within the defect-molecule concept, we have to consider V^- as a five-electron system.[3,24] Taking five-electron states, the ground state of Fig. 11 is

$$|\psi_0\rangle = |a_1'\bar{a}_1'a_1''\bar{a}_1''b_1\rangle , \tag{12a}$$

where the bar denotes an electron in a state with opposite spin. The energy of this ground state is called ε_0. There exist four excited states with the same symmetry (Fig. 11):

$$|\psi_1\rangle = |a_1'\bar{a}_1'b_2\bar{b}_2b_1\rangle , \tag{12b}$$

$$|\psi_2\rangle = |a_1''\bar{a}_1''b_2\bar{b}_2b_1\rangle , \tag{12c}$$

$$|\psi_3\rangle = |a_1'\bar{a}_1''b_2\bar{b}_2b_1\rangle , \tag{12d}$$

$$|\psi_4\rangle = |a_1''\bar{a}_1'b_2\bar{b}_2b_1\rangle . \tag{12e}$$

By configuration interaction these excited states are mixed into the ground state. The energies of these excited states are called ε_1 to ε_4. Figure 12 shows the level scheme of this many-electron system. Only the states $|\psi_3\rangle$ and $|\psi_4\rangle$ have spin density on the *bc* plane. The levels belonging to these states are, in first order, degenerate. By spin-spin interaction, however, the spin-up levels of Fig. 11 are lowered with respect to the spin-down levels, due to the spin-up b_1 level. This causes the many-electron levels ε_3 and ε_4 of Fig. 12 to split, leading to a different amount of mixing into the ground state. Due to this difference, an unbalance between spin-up and spin-down can result on the *bc* plane. This problem has been treated in some quantitative detail by Lannoo.[29] He derives an expression for the spin density on the *bc* plane as a function of the splitting parameters of the one-electron picture (Fig. 11) and the parameter λ. This parameter λ turns out to play a crucial role. Another parameter entering is the many-electron potential describing the importance of the many-electron effects. The main conclusion of Lannoo is that

correlation effects (configuration interaction) can indeed account for a value of 2.1 MHz on the *bc* plane. For λ, a value 0.9 results, if it is assumed that the hyperfine tensor M*bc* 1 belongs to atoms *b* and *c* and when only the isotropic part of the hyperfine interaction is considered.

This treatment very clearly shows, qualitatively, the mechanisms that lead to an effect such as the one observed. However, one should be careful when interpreting the figures quantitatively. For instance, the many-electron potential enters to the third power in the expression for the spin density on the *bc* plane,[29] whereas its magnitude is estimated on purely theoretical grounds, without any experimental verification. Moreover, in the theory the derived spin density is, in terms of the dangling bonds, proportional to $(b+c)^2$. That means that on the *b* and *c* atoms the resulting hyperfine interaction is expected to be ⟨111⟩ axial, as is the hyperfine interaction on the nearest neighbors *a* and *d*, from an $(a-d)$-type wave function. From the experimental results one can verify, that none of the five M*bc* tensors observed has this ⟨111⟩ axial character.

There is still a more general more-electron effect that deserves attention. Even if, to first order, the density of the unpaired electron on the *bc* plane vanishes by symmetry, a source of net spin density can be found when considering the effect of exchange interaction between the unpaired defect electron and the closed shell electrons of the atoms in this plane. We should include here all electrons, 1*s*, 2*s*, and 2*p* core states, and the $(3s)(3p)^3$ hybridized valence electrons. Mostly these effects are rather small,[30] but they can be expected to be seen in a system such as V^-, where in a region very close to the vacancy symmetry requires a vanishing density of the unpaired defect electron. An excellent example of such a system in an ionic crystal is the V_K center in LiF which could also theoretically be explained.[31,32] As these exchange polarization effects can be of either sign, they offer a possible explanation for contact interactions of reversed sign. They may also contribute to an apparently larger than 100% localization of the unpaired defect electron.

D. Further lattice site assignments—dipole-dipole effects

As described in Sec. I F, the anisotropic part of hyperfine tensors $\overleftrightarrow{B}$ can be interpreted as arising from dipole-dipole interaction between the magnetic moments of the nucleus and the electronic spin distribution [Eq. (6)]. In the usual LCAO practice in silicon, $\overleftrightarrow{B}$ primarily originates from a *p*-like wave function on the nucleus itself. Strictly, however, one should include the total electronic wave function Ψ in Eq. (6), thus also orbitals from neighboring sites. These effects have been neglected in the results of Table IV, since in most cases in silicon these contributions are small compared to the contributions of its own orbitals, due to the r^{-3} character of Eq. (6).

In the case of V^-, this situation is different for some atom positions. Due to the antisymmetric character of

TABLE VI. Comparison of calculated and experimental values for anisotropic hyperfine interactions. "expt" are the experimental values, "PC [*xyz*]" are values calculated at site [*xyz*] as a result of point charges at four chain positions, and, "orb [*xyz*]" are values calculated for Slater-type orbitals with parameter values $\alpha_s=1.87$ and $\alpha_p=1.60$ (Ref. 33). As the tensors are traceless, $B_{xx}=-B_{yy}-B_{zz}$ is omitted. Units are kHz.

Tensor	B_{yy}	B_{zz}	B_{xy}	B_{xz}	B_{yz}	Remarks
expt T1	−74.1	$=B_{yy}$	0.0	0.0	32.3	$a=-666.2$ kHz
PC [$\bar{4}00$]	−71.5	$=B_{yy}$	0.0	0.0	28.8	
orb [$\bar{4}00$]	−75.9	$=B_{yy}$	0.0	0.0	17.5	
expt T2	−16.1	$=B_{yy}$	0.0	0.0	49.3	$a=-282.7$ kHz
PC [400]	−24.9	$=B_{yy}$	0.0	0.0	5.9	$\vec{B}_{\text{expt}}-\vec{B}_{\text{orb}}$
orb [400]	−31.1	$=B_{yy}$	0.0	0.0	4.6	is [011] axial
expt M*bc* 5	−394.8	$=B_{yy}$	−664.2	$=-B_{xy}$	−211.2	$a=203.8$ kHz
PC [$1\bar{1}1$]	−30.5	$=B_{yy}$	−119.1	$=-B_{xy}$	16.6	
orb [$1\bar{1}1$]	−47.6	$=B_{yy}$	−194.9	$=-B_{xy}$	−28.9	
orb [$1\bar{1}1$]	−343.0	$=B_{yy}$	−584.2	$=-B_{xy}$	−136.9	Distorted
expt M*bc* 1	−92.7	$=B_{yy}$	195.8	$=-B_{xy}$	13.3	$a=2105.8$ kHz
PC [$\bar{3}\,\bar{1}\,1$]	−39.8	$=B_{yy}$	117.7	$=-B_{xy}$	4.2	
orb [$\bar{3}\,\bar{1}\,1$]	−63.9	$=B_{yy}$	124.3	$=-B_{xy}$	−17.2	
expt G22	−42.4	99.9	−24.9	38.1	−53.9	$a=322.5$ kHz
PC [004]	−37.8	100.6	−11.4	45.2	−54.9	
orb [004]	−48.1	117.8	−7.7	36.6	−40.5	
expt G26	−32.7	73.0	1.2	−5.1	−2.1	$a=239.3$ kHz
PC [$\bar{1}15$]	−39.3	81.0	2.6	−8.6	−1.3	
orb [$\bar{1}15$]	−36.0	74.3	1.0	−10.2	4.5	

the wave function, spin densities on or near the (011) plane will be small with yet a large anisotropic spin distribution nearby: the atoms a and d, each carrying $\sim 30\%$ of an electron with unpaired spin.

In order to make an estimate of the effect for a comparison with the experimental values, we have to calculate integrals of Eq. (6) for the atom positions on or near the (011) plane. For Ψ we take the orbitals found by analysis of the largest Mad tensors, as given in Table IV. We will limit ourselves to the shells Mad1 and Mad2. The simplest representation of the orbitals is, of course, to treat them as point charges with an electronic fraction η^2. In that case the integrals of Eq. (6) become very simple and the contribution of each of the four atom positions consists of a purely axially symmetric $\overleftrightarrow{B}$ tensor yielding a b value

$$b=\eta^2\frac{\mu_0}{4\pi}g\mu_B g_N\mu_N\frac{1}{r^3} \tag{13}$$

and an axial direction along the connection line between the atom position and the nucleus. Addition of these four $\overleftrightarrow{B}$ tensors in the Cartesian coordinate system yields a (generally nonaxial) $\overleftrightarrow{B}$ tensor, to be compared with experimental tensors.

In a more sophisticated treatment one can take Slater-type orbitals. By symmetry, there is still an ambiguity in the directions of the orbitals, caused by the (011) mirror plane. It is assumed, however, that all orbitals point toward the vacancy. The integration over these orbitals is easy when using the series expansion derived by Ammerlaan and Wolfrat.[33] Results of these calculations for some atom positions are given in Table VI.

First we will discuss the results of the calculation for the two nearest T-class lattice positions [$\bar{4}$00] and [400]. It is very probable that they have to be compared with the two observed T-shell tensors, as the next T positions lie as far as [$\bar{8}$00] and [800]. From Table VI it is clear that the results for the point-charge model and the orbital model are not appreciably different. This gives one confidence that the precise structure of the orbitals is not too important here. When comparing this to experimental data we must remember that no absolute signs could be determined from the ENDOR measurements. Thus, in Table VI the sign is chosen for best agreement with the calculations, resulting sometimes in a change of sign for a.

Tensor T1 matches very well with the [$\bar{4}$00] position, with $a=-666.2$ kHz. For T2 the match is not very good. Also, here the best result can be obtained when taking a negative a. In that case the difference between the experimental and the orbital-calculated tensors is a [011] axial tensor with $b=29.9$ kHz and $c=0.2$ kHz. Such a [011] axial traceless tensor is the only kind of tensor that gives, in a LCAO analysis, a function with antisymmetric character with respect to the (011) plane. Such a wave function is allowed even in the one-electron treatment. The value of η^2 belonging to this b value is only 0.026%. Yet, these identifications are tentative.

As the approach turns out to be not unreasonable, it is worthwhile to try to match some of the Mbc tensors. The most important Mbc tensors seem to be Mbc5, with the largest anisotropy, and Mbc1, with the largest trace. Intuitively, Mbc5 seems a candidate for the nearest-neighbor position c of the vacancy, [1$\bar{1}$1]. In Table VI one can see that the match is very poor. The calculated values are up to a factor of 10 too small. By a lattice distortion in the inward direction the calculated values can be made to match with the experimental values. Figures for a best fit are also given in Table VI. We believe, however, that the required distortions are unreasonably large: all four neighbor atoms have to move inward over 0.8 Å, the a atom to (−0.83,0.57,0.57), the c atom to (0.83,−0.60,0.60). Besides being too large, these distortions are probably in the wrong direction, as theoretical estimates for the symmetric, or breathing, distortion mode give figures of 0.1 to 0.3 Å in the outward direction for V^0.[10,34–36] It is clear that for the very close, nearest-neighbor Mbc positions the differences between the point-charge and orbital models are no longer negligible and thus strongly dependent on the true shape of the orbitals. Slater orbitals tend to give here a too localized representation. Moreover, other sources of spin density around the nearest-neighbor atoms have to be considered, e.g., exchange (core) polarization. For the match between Mbc1 and the more remote lattice position [$\bar{3}\,\bar{1}$1], the agreement is much better, as can be verified in Table VI.

Inspection of the G-class tensors reveals that two of them, G22 and G26, can be calculated with reasonable accuracy by dipole-dipole interaction. Both positions, at [004] and [$\bar{1}$15], lie in the second plane of atoms above the Mad symmetry plane; perhaps that is the explanation why the transferred charge to these sites is only small, compatible with the one-dimensional extent of the wave function as inferred in Sec. III B.

It is clear that dipole-dipole interaction between the unpaired defect electron and certain nuclei can lead to a tentative assignment to lattice positions (marked dd in Table IV) for several of the 51 hyperfine tensors.

IV. THE POSITIVE VACANCY

After the determination of hyperfine parameters of Si:V^-, it was tempting to try ENDOR on the other paramagnetic charge state of the monovacancy in silicon, V^+. For several reasons this defect has gained even more theoretical attention. Firstly, the electronic structure counts only three electrons. Furthermore, only one (tetragonal) Jahn-Teller distortion is involved. These are reasons why calculations will, in general, be simpler. In recent years, especially the negative-U character of this defect and thus its metastability triggered much theoretical interest.

TABLE VII. Hyperfine parameters for the partially resolved shells of the positively charged vacancy as determined from EPR measurements in the [100] direction. Units are MHz.

Tensor	A_{xx}	A_{yy}, A_{zz}	No. of atoms
M1	113 ±1	101 ±1	4
M2		3.9±0.2	4
G1	9.6±0.5	7.5±0.1	8

In the same cryostat as was used for V^- we produced V^+ by electron irradiation of boron-doped material (0.1 Ω cm, 5×10^{17} B atoms cm^{-3}). The high doping level was chosen in order to keep the Fermi level low, to allow the positive charge state to arise. For unknown reasons we were not able to convert a substantial fraction of the vacancies to the positive charge state. We observed the Si-G1 spectrum ascribed to V^+, but never in a concentration exceeding $(1-5)\times10^{15}$ cm^{-3}. An even greater problem was the failure to detect any ENDOR effect at temperatures from 2 to 15 K and at various microwave power levels. Above 15 K even the EPR spectrum disappears. This failure seems to be related to the spin-lattice relaxation, which is very fast, even at 2 K (see the discussion in Sec. I C). There is a chance, however, that both problems (low conversion to V^+ and fast spin-lattice relaxation) are at least partly caused by the low resistivity of the material, which has free carriers even at low temperatures. From the disturbance of the electric field in the microwave cavity we concluded that so-called impurity-band conduction was present in the sample, at least in the earlier stages of the irradiation.

From the EPR measurements we were able to determine part of the hyperfine structure in more detail than published before.[1] Due to the overlap with other strong EPR spectra (Si-G6, Si-G28, and Si-G2), hyperfine parameters for three hyperfine shells could only be determined in the [100] direction. Because of the importance of the defect, these results, though incomplete, are presented in Table VII. One interesting feature can already be derived from these figures. As for $\langle 111\rangle$ axial tensors $A_{xx}\simeq A_{yy}\simeq A_{zz}$, the tensors M1 and G1 turn out to be appreciably less $\langle 111\rangle$ axial than the M*ad* 1 and G1 tensors of V^-.

V. CONCLUSIONS

This study demonstrates that the use of ENDOR as a spectroscopic technique can yield an extremely detailed set of hyperfine parameters. The ENDOR results confirm the picture of the structure of the vacancy in silicon that was developed by Watkins based upon EPR studies.

Since of all the defects in semiconductors, the vacancy has been studied the most intensively by theoretical methods, one would expect that tools should be on hand to interpret the present ENDOR data in terms of the electronic structure. None of the nearly 100 theoretical papers, however, presents sufficiently detailed and realistic results to serve as a direct comparison with the present data. Therefore, in Sec. III, a more phenomenological interpretation was given. Detailed theoretical calculations are beyond the scope of this experimental study.

We showed that the defect has a nearly one-dimensional character due to the preference of the charge for {110} coplanar atom chains. Furthermore, it was demonstrated that the experimental data show some of the features expected for a wave function which has a distinct nodal plane. Several hyperfine tensors are known to originate from sites in this nodal plane. The fact that these hyperfine interactions are small compared to the hyperfine interactions from the *a* and *d* atoms does not mean that they are less important: among the M*bc*-type tensors is the interaction with the first neighbors *b* and *c*. This is another example of the power of the ENDOR technique. Through the high resolution, not only the hyperfine interactions that arise from atom shells that are far away from the defect (and therefore perhaps less important) are revealed, but in some cases also very important shells are resolved of which the hyperfine interactions are small for symmetry reasons. Here ENDOR provides quantitative information that can be used in the estimation of the importance of many-electron effects.

The LCAO description of the wave function of the vacancy is found to give a reasonable description for the observed hyperfine interactions for a majority of the lattice sites. Near the nodal plane of the wave function other effects are found to be prominent. Dipole-dipole interaction with spin density on nearby lattice sites gives rise to nonaxial interactions. Exchange polarization can cause contact interactions of opposite sign. On the other hand, it can also contribute to the apparently more than 100% localization, as found in the LCAO analysis.

On the basis of the chain model and of calculated dipole-dipole effects, 21 of the 51 hyperfine tensors could be assigned to shells of lattice positions. Some of these assignments we consider as reliable, others as rather tentative. In order to further test the ideas developed here, a highly similar defect, the negatively charged oxygen-vacancy complex, has been studied in the same way.[37]

---

*Present address: Free University Hospital, Postbus 7057, 1007 MB Amsterdam, The Netherlands.

[1]G. D. Watkins, J. Phys. Soc. Jpn. **18**, Suppl. II, 22 (1963).

[2]G. D. Watkins, in *Radiation Damage in Semiconductors,* edited by P. Baruch (Dunod, Paris, 1965), p. 97.

[3]G. D. Watkins, in *Radiation Damage and Defects in Semiconductors 1972,* edited by J. E. Whitehouse (Institute of Physics, London, 1973), p. 228.

[4]G. D. Watkins, in *Lattice Defects in Semiconductors 1974,* edited by F. A. Huntley (Institute of Physics, London, 1975), p. 1.

[5]G. D. Watkins and J. R. Troxell, Phys. Rev. Lett. **44**, 593 (1980).

[6]G. D. Watkins, A. P. Chatterjee, and R. D. Harris, in *Defects and Radiation Effects in Semiconductors 1980,* edited by R. Hasiguti (Institute of Physics, London, 1981), p. 199.

[7]J. L. Newton, A. P. Chatterjee, R. D. Harris, and G. D. Watkins, Physica B **116**, 219 (1983).

[8]M. Sprenger, Ph.D. thesis, University of Amsterdam, 1986 (available through the authors).

[9]G. A. Baraff, E. O. Kane, and M. Schlüter, Phys. Rev. Lett. **43**, 956 (1979).

[10]G. A. Baraff, E. O. Kane, and M. Schlüter, Phys. Rev. B **21**, 5662 (1980).

[11]G. A. Baraff, E. O. Kane, and M. Schlüter, in *Defects and Radiation Effects in Semiconductors 1980,* edited by R. Hasiguti (Institute of Physics, London, 1981), p. 19.

[12]J. G. de Wit, E. G. Sieverts, and C. A. J. Ammerlaan, Phys. Rev. B **14**, 3494 (1976).
[13]E. G. Sieverts, S. H. Muller, and C. A. J. Ammerlaan, Phys. Rev. B **18**, 6834 (1978).
[14]K. L. Brower, Phys. Rev. B **1**, 1908 (1970).
[15]G. D. Watkins, Phys. Rev. B **12**, 5824 (1975).
[16]M. Sprenger, E. G. Sieverts, S. H. Muller, and C. A. J. Ammerlaan, Solid State Commun. **51**, 951 (1984).
[17]G. H. Fuller, J. Phys. Chem. Ref. Data **5**, 835 (1976).
[18]E. G. Sieverts, Ph.D. thesis, University of Amsterdam, 1978, Appendix A.
[19]The fitting programs are based on the routine ZXSSQ from the FORTRAN library IMSL. Information on the program library EPRLIB is available on request, from Dr. C. A. J. Ammerlaan.
[20]J. R. Morton and K. F. Preston, J. Magn. Reson. **30**, 577 (1978).
[21]F. Herman and S. Skillman, *Atomic Structure Calculations* (Prentice Hall, Englewood Cliffs, NJ, 1963).
[22]G. D. Watkins and J. W. Corbett, Phys. Rev. **134**, A1359 (1964).
[23]M. Sprenger, R. van Kemp, E. G. Sieverts, and C. A. J. Ammerlaan, J. Electron. Mater. **14A**, 815 (1985), and following paper, Phys. Rev. B **35**, 1582 (1987).
[24]M. Sprenger, S. H. Muller, and C. A. J. Ammerlaan, Physica B **116**, 224 (1983).
[25]G. D. Watkins and J. W. Corbett, Phys. Rev. **121**, 1001 (1961).
[26]E. G. Sieverts, J. Phys. C **14**, 2217 (1981).
[27]M. Lannoo and P. Lenglart, J. Phys. Chem. Solids **30**, 2409 (1969).
[28]E. O. Kane, Phys. Rev. B **31**, 5199 (1985).
[29]M. Lannoo, Phys. Rev. B **28**, 2403 (1983).
[30]R. E. Watson and A. J. Freeman, in *Hyperfine Interactions*, edited by A. J. Freeman and R. B. Frankel (Academic, New York, 1967), p. 53ff.
[31]R. Gazzinelli and R. L. Mieher, Phys. Rev. **175**, 395 (1968).
[32]D. Ikenberry, A. N. Jette, and T. P. Das, Phys. Rev. B **1**, 2785 (1970).
[33]C. A. J. Ammerlaan and J. C. Wolfrat, Phys. Status Solidi B **89**, 541 (1978).
[34]F. P. Larkins and A. M. Stoneham, J. Phys. C **4**, 143 (1971); **4**, 154 (1971).
[35]U. Lindefelt, Phys. Rev. B **28**, 4510 (1983).
[36]M. Scheffler, J. P. Vigneron, and G. B. Bachelet, Phys. Rev. B **31**, 6541 (1985).
[37]R. van Kemp and C. A. J. Ammerlaan (unpublished).